

Impact of juxta-anastomotic stent implantation on the haemodynamics within a single representative patient AVF

Sanjiv Gunasekera^{a,*}, Olivia Ng^a, Shannon Thomas^b, Ramon Varcoc^b, Charitha de Silva^a, Tracie Barber^a

^a School of Mechanical and Manufacturing, The University of New South Wales, 2052 NSW, Australia

^b Prince of Wales Hospital, Randwick, 2031 NSW, Australia

ARTICLE INFO

Keywords:

Haemodynamics
Arteriovenous fistula
Stent
CFD
Malapposition

ABSTRACT

An arteriovenous fistula (AVF), a vascular structure surgically created to enable haemodialysis, is commonly affected by stenosis in the juxta-anastomotic region. A new treatment involving the implantation of a flexible stent has shown good potential for retaining healthy AVFs. Since vascular disease in the AVF is known to be related to the haemodynamic environment within the vasculature, this study aims to understand the impact of the stent implantation on the flow dynamics within a single patient-specific AVF. A virtual stented geometry of the AVF was obtained with micro-CT images of a benchtop AVF model implanted with a Supera stent. Reynolds averaged Navier–Stokes simulations were conducted with physiological boundary conditions (Reynolds numbers varying from 345 to 730) applied on the AVF model with and without the presence of the stent. Velocity contour slices within the vein showed the concentration of high velocity in the stent encapsulated region. Moreover, the ratios of flow rate across the stent-lumen cross-sections over the flow rate across the vessel-lumen cross-sections suggested that the flow was being funnelled through the stent encapsulated regions of a malapposed section, despite the porous structure of the stent. A larger low velocity recirculation region translated to a larger vessel wall area of high Oscillatory Shear Index (OSI) and low Time-Averaged Wall Shear Stress (TAWSS) in the AVF model with the stent absent, compared to the stented model. This suggested that the adverse haemodynamic behaviour was being funnelled away from the vessel wall, possibly leading to a protective environment in the malapposed region of the vein.

1. Introduction

End Stage Renal Disease (ESRD) is the final stage of Chronic Kidney Disease (CKD), where the filtration ability of the kidneys have ceased, necessitating renal replacement therapy to keep the patient alive. Although kidney transplantation is associated with lower mortality rates (Tonelli et al., 2011), haemodialysis is the most common treatment option (TSANZ, 2019) where transplantation is largely limited by organ availability (ANZDATA, 2018). Haemodialysis vascular access is established by the creation of an arteriovenous fistula (AVF) which is a surgical connection between a vein (usually the cephalic vein in the forearm) and an artery (usually the adjacent radial artery). This short-circuit of the peripheral vascular network increases the blood flow rate and diameter of the vein, enabling a quicker and efficient dialysis process while providing an easier and more robust access point for cannulation (Konner et al., 2003).

The AVF is affected by numerous complications (Al-Jaishi et al., 2017), of which narrowing of the vasculature is most common. The juxta-anastomotic region (defined as the inflow artery and vein within 5 cm of the anastomosis) is the most common site of stenosis formation (Stolic, 2013), often caused by Intimal Hyperplasia (IH) (Duque et al., 2017). Although the exact mechanism that initiates IH is elusive, it is understood that upstream events such as haemodynamic factors and surgical stressors (among other pathogenetic factors) lead to the downstream biological responses such as the production of various cellular and molecular level regulators (Roy-Chaudhury et al., 2006). Disturbed flow regions, such as recirculation zones, coupled with low flow have been known to be co-located with regions of vasoconstrictive cell responses (Chiu and Chien, 2011). Computational (Remuzzi and Ene-Iordache, 2013; Bozzetto et al., 2016) and benchtop fluid dynamic (Kharboutly et al., 2010; Gunasekera et al., 2020) experiments on patient-specific models have demonstrated recirculating flow in the

* Corresponding author.

E-mail address: s.gunasekera@unsw.edu.au (S. Gunasekera).

<https://doi.org/10.1016/j.ijheatfluidflow.2021.108874>

Received 20 May 2021; Received in revised form 10 September 2021; Accepted 5 October 2021

Available online 20 November 2021

0142-727X/© 2021 Elsevier Inc. All rights reserved.

juxta-anastomotic region with transitional flow initiating in the anastomosis.

Salvaging the stenosed AVF may involve the use of endovascular methods, such as angioplasty or stent implantation, and in some cases, open surgical repair (Lok et al., 2020). Although stent implantation was initially a contested method of treating diseased AVFs, current studies have shown that the advancement in stent technology has yielded better clinical outcomes in comparison to angioplasty alone (Fu et al., 2015). Particularly, the use of flexible stents across the anastomosis has yielded high unassisted primary patency (Swinnen et al., 2015; Thomas et al., 2019). However, malapposition of the stent to the vessel wall is possible in this region, as illustrated in Fig. 1.

An undersized stent implantation is known to be a predictor of stent thrombogenicity (Van Werkum et al., 2009) and the malapposition of the stent has shown to produce recirculation regions near stent struts, along with increasing areas of low Time-Averaged Wall Shear Stress (TAWSS) (Chen et al., 2017). However, with the increase in the degree of undersizing beyond 5% of the vessel diameter (equivalent to a decrease in stent lumen area below 90.25% of the vessel lumen) a decrease in the heterogeneity of the wall shear stress (WSS) was evident across the vessel (Chen et al., 2009). A recent study has shown that undersized stent-grafts used to treat cephalic arch stenoses associated with AVFs, have yielded higher access patency rates and a decrease in interventions (Huang et al., 2020).

In summary, the juxta-anastomotic stent implantation treatment is capable of retaining functioning AVFs but has the potential for the malapposition of the stent to occur within the vein. Fluid dynamic studies considering low levels of malapposition have shown adverse WSS patterns while presenting the tendency for smoother patterns with the increase in malapposition. The aim of the current study is to observe the influence of a juxta-anastomotic stent implantation on the bulk flow features within a single representative patient-specific AVF.

2. Methodology

2.1. Geometry preparation

A patient AVF, that had undergone juxta-anastomotic stent treatment, was scanned with approval of the South Eastern Sydney Local Health District-Human Research Ethics Committee. The geometry was noted by the clinician authors, with long-term experience in the field of vascular access, to be representative of the typical AVF geometry. A volume of ultrasound scans of the patient AVF was obtained by using a freehand ultrasound scanning procedure (Colley et al., 2018). The scan volume was segmented to produce the patient-specific vessel geometry in the STL surface mesh file format which was subsequently 3D printed with a PVA filament, using an Ultimaker 3 (Ultimaker BV). A polydimethylsiloxane (PDMS) model of the geometry was fabricated by casting the Sylgard 184 (Dow Inc.) silicone around the 3D printed model, using an elastomer to curing agent ratio of 22.5:1 to make the silicone model more elastic. The PVA 3D print was dissolved by flushing the model with water to create a phantom of the patient-specific AVF

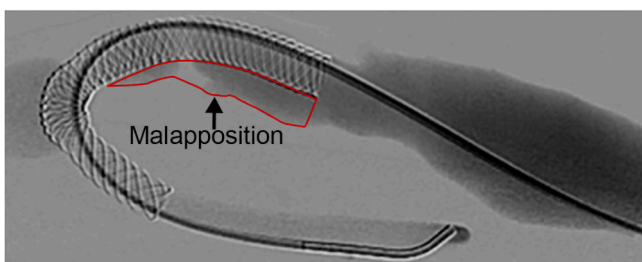


Fig. 1. An angiogram of a juxta-anastomotic stent implanted Arteriovenous Fistula with malapposition of the stent. Adapted from Thomas et al. (2019).

vessels.

A 5mm diameter Supera stent (Abbott Vascular, Santa Clara, CA, USA), the same size of which was implanted in the patient's AVF, was also deployed (by a vascular surgeon) into the PDMS model. On observation, after the stent implantation, it was apparent that there was a level of malapposition of the stent in the venous segment close to the anastomosis. Malapposition of this nature and degree has been noted in clinical circumstances by the clinician authors and has been observed in cases where the vein is of a large diameter (Thomas et al., 2019) as can be seen in the example angiogram image shown in Fig. 1.

The initial ultrasound scan volume could not be used to segment the stent due to the presence of excessive artefacts in the scans and the lack of resolution of the scans to pick up the detail of the stent. To obtain a precise rendering of the stent implanted AVF model, a micro-CT scanner (MILabs U-CT at MWAC, UNSW Sydney), was used to obtain an ultra-focus scan at an approximate overall resolution of 20 μm . The resulting high-resolution scan volume was segmented to generate an STL of the stent geometry and the segmentation of the vessel geometry was repeated to locate the AVF vessels in the same local coordinate system of the stent STL, as illustrated in Fig. 2. In order to isolate the impact of the stent, two geometries, with and without the stent present, were used for the simulations. The stent implanted vessel geometry without the physical stent present is referred to as the 'stent-absent' geometry whereas the geometry with the stent present will be referred to as the 'stented' geometry.

The stent and vessel geometries were smoothed using several iterations of a Gaussian smoothing algorithm. To ensure the stent strut diameter was equivalent to 152 μm (the physical stent strut diameter), sections of the segmented stent radius were measured using a Matlab (Mathworks Inc.) algorithm by calculating the distance between the stent strut centerline and the closest STL surface elements. This algorithm was used after each smoothing iteration to ensure an appropriate level of surface smoothness was achieved whilst avoiding overly shrinking the stent STL.

To assist with visualising the flow within the vein of the AVF, cross-sections of the vessel lumen were created by generating planes perpendicular to the centerline such that the slices conformed with the tortuous nature of the patient-specific geometry. To understand the effect of the malapposition of the stent in the vein, additional slices were manually created to represent the subspace of the slices that were encompassed by the stent, here forth referred to as the stent lumen slices. The inset image of Fig. 2 illustrates the two types of lumen slices and their locations.

2.2. Computational fluid dynamics settings

The Reynolds Averaged Navier Stokes (RANS) equations were solved using the Fluent 19.2 (ANSYS Inc.) software package. The fluid region of the AVF geometry was discretized by creating a tetrahedral mesh in the bulk flow and boundary layer regions using ICEM CFD (ANSYS Inc.). Tetrahedral cells were used, even in the boundary layer region, because of the complexity of the geometry which incorporated the small intertwining surface of the stent within the relatively larger vessel surface. The average cell distance from the wall was 18.04 μm (equivalent to a y^+ of 0.22) which enabled accurate wall shear stress measurements. Grid convergence was assessed using circumferentially averaged wall shear stress (WSS) values at 5 slices in the vein and an average grid convergence index of 5.28% was calculated showing that a sufficient level of spatial resolution of the grid was achieved with a mesh of approximately 20 million elements.

In addition to the ultrasound scans, the patient flow rates of the feeding vessels of the AVF were also recorded using Spectral Doppler ultrasound (Carroll et al., 2020). The recorded flow rates were digitized in order to use as pulsatile inlet flow waveforms at the proximal artery (PA) and the distal artery (DA) ends of the AVF. These inlet waveforms resulted in Reynolds numbers varying from 345 to 730 which gave an

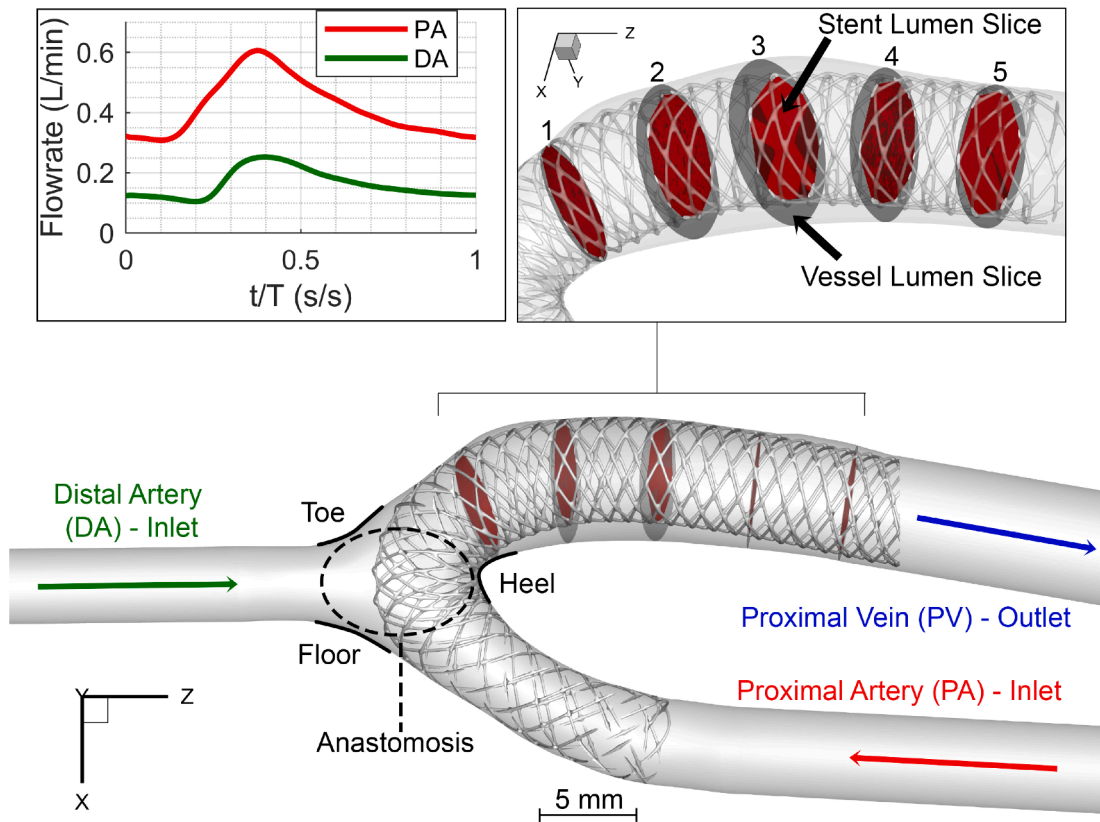


Fig. 2. The overview of the simulation. The AVF geometry with the stent implantation is shown in the central image. Parts of the anastomosis and inlet/outlet vessels have been annotated. The inset image at the top left is of the inlet flowrate waveforms. The inset image at the top right illustrates the stent lumen and vessel lumen slices.

outlet Reynolds number varying from 507 to 1031. The recorded heart rate of the patient was 60 bpm which was matched in the simulations by setting the period of the inlet waveforms to 1 s. The proximal vein (PV) was maintained as a non-tractive outlet condition with relative pressure held at zero. To ensure the inlet flow waveforms had a developed flow profile, the ends of the vessels were extended by 10 times the diameters of the relevant vessel.

The vessel and stent walls were set up with a no-slip wall condition and without compliance. We note a comparison between a stationary wall to a compliant wall in AVF flow simulations have shown that the resulting WSS trends remain similar with a general overestimation of the values at regions of low WSS in the case of the stationary wall (McGah et al., 2014). The fluid properties were set to replicate the average blood physical properties with a density of 1060 kg/m^3 . The effect of the non-Newtonian nature of blood, known to be minimal at the high shear rates (Vijayaratnam et al., 2015) encountered in an AVF, was modelled using the Carreau model (Cho and Kensey, 1991). The model parameters: zero-shear rate viscosity, infinite-shear rate viscosity, characteristic time and power-law index were set to 0.056 Pa·s, 0.00345 Pa·s, 3.313s and 0.3568, respectively.

The transient simulations were conducted with a fixed time-step of 0.001 s. The time-step was deemed appropriate after obtaining an average variation of 0.70% in WSS values across the vein when compared with values obtained with a time-step of an order of magnitude lower. To model the turbulent behaviour in the AVF, the $k-\omega$ SST turbulence model, which has been shown to perform well in transitional flows within vasculature (Tan et al., 2008), was implemented.

3. Results and discussion

3.1. Flow features within the vein

The simulation was run for four cycles and the flow features were analysed using the data from the final cycle. Velocity streamlines coloured with the velocity magnitude were plotted at the maximum and minimum points of the inlet flow profile for both the stented and stent-absent geometries, as seen in Fig. 3. In both geometries and at both time points, a high flow central region enveloped by spiralling low flow is apparent. The first few spiralling streamlines in the stented geometry realigns with the outflow direction, closer to the anastomosis than the first spiralling streamlines of the stent-absent geometry. The delay in reattachment could be related to the extent of the recirculating region seen in the vein close to the heel of the anastomosis. The recirculating flow in the stent-absent geometries at both time points are much larger compared to those in the stented geometry. A tomographic particle image velocimetry study of the stent-absent geometry showed similar behaviour where the flow in the anastomosis was enveloped by spiralling flow (Gunasekera et al., 2020). A recirculation zone was also noted in the lower region of the vein, further aligning with the observations in the current study.

Contour plots of the velocity magnitude were plotted on the vessel lumen slices to observe the central flow features of the vein with clarity as illustrated in Fig. 4. The high velocity is distributed in the upper outer regions of the slices in both geometries. This distribution when combined with the observations of the streamlines, suggest the presence of two counter-rotating spirals originating from the anastomosis and traversing across the juxta-anastomotic region of the vein. Although this feature is maintained throughout all the slices (most distinctly apparent at the maximum inlet flow time point), the high velocity magnitude is

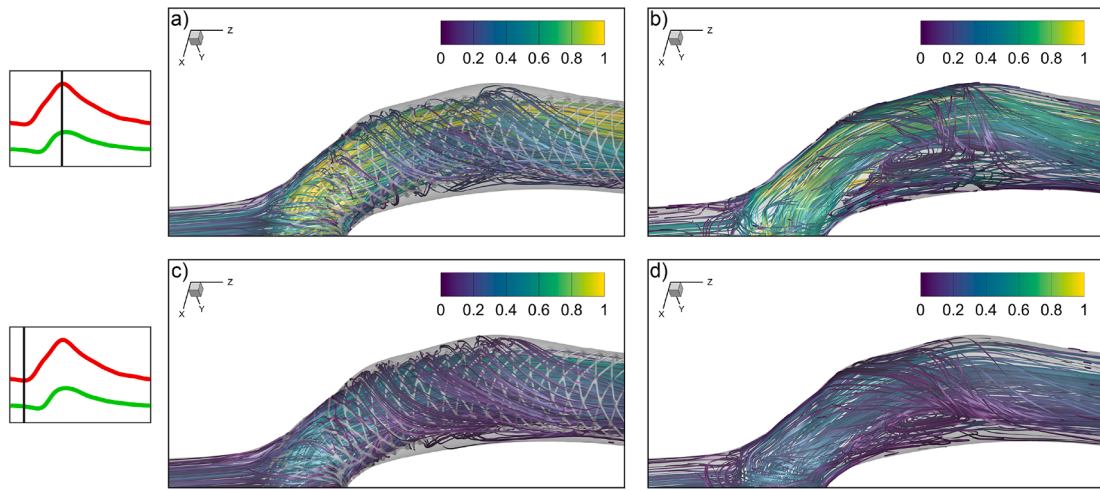


Fig. 3. Velocity streamlines coloured with the velocity magnitude at the maximum (subfigures a) and b)) and minimum points (subfigures c) and d)) of the inlet flow profile. The subfigures a) and c) are of the stented geometry while the subfigures b) and d) are of the stent-absent geometry.

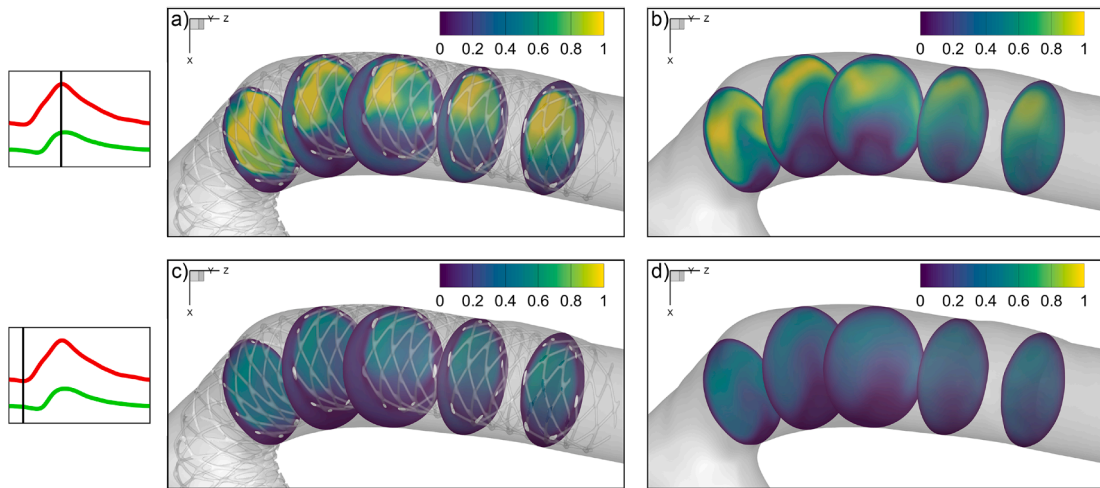


Fig. 4. Velocity magnitude contours at the 5 vessel lumen slices at the maximum (subfigures a) and b)) and minimum points (subfigures c) and d)) of the inlet flow profile. The subfigures a) and c) are of the stented geometry while the subfigures b) and d) are of the stent-absent geometry.

maintained for longer in the stented geometry.

A low velocity region is apparent at the lower border of the vessel lumen slices. Much like the observations made with the streamlines, the low velocity region is of a larger spread in the stent-absent geometry where it reaches the fourth slice, whereas the region is not visible beyond the second slice in the stented geometry. The low velocity region coincides with the region of recirculating flow in the stent-absent geometry. Previous studies have postulated that low velocity recirculating flow could be related to the onset of vascular disease (Gimbrone and García-Cardena, 2016; Remuzzi and Ene-Iordache, 2013; Ishibashi et al., 1995).

Another less distinct feature that can be seen in the slices of the stented geometry is the presence of a second low velocity region at the lower section of the stent lumen slices. This secondary low flow section extends towards the third slice as well. Together with this, the high velocity central region is maintained for a longer distance within the stented geometry as opposed to the high flow in the stent-absent geometry which spreads throughout the vessel after slice 2. Furthermore, the high flow region in the stented geometry is encapsulated by the bounds of the stent thereby suggesting that the flow is concentrated within the stent.

3.2. Flow rate ratios across stent and vessel lumen slices

To quantify the concentration of flow within the stent encapsulated region of the flow domain, stent lumen slices were created in the subspace of vessel lumen slices at 5 locations as seen in Fig. 2. The flowrate across both the vessel lumen slice and the stent lumen slice was measured for both the stented and stent-absent geometry at the 5 locations. The ratio of the flow rates across the stent lumen slice and the vessel lumen slice at each location was averaged temporally and compared against each other in Fig. 5. Along with the flow rate ratios, the area ratios between the stent lumen slices and the vessel lumen slices were also calculated to provide an indication of the level of malapposition at these locations. There is a significant level of malapposition at the slice number 3, where only approximately 54.3% of the vessel lumen is captured by the stent; the flow rate ratios also are lowest at slice number 3. The trend of the flow rate ratios decreasing with the increase in malapposition (i.e. slices 1 and 2) and vice versa (i.e. slices 4 and 5) is seen with both geometries. However, the most important finding is that the flow rate ratio of the stented geometry incurs a decrease from 98.6% to 84.3% (14.3% change) in the first three slices whereas the decrease in the stent-absent geometry is much larger where the flow rate ratios drop from 92.4% to 67.5% (24.9% change). On average across all slices, the

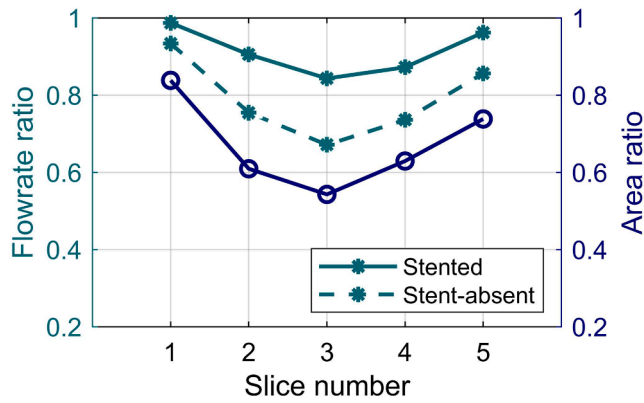


Fig. 5. Cycle-averaged ratios of flow rate across the stent lumen slice and the vessel lumen slice at five locations in the vein in both stented and stent-absent geometries along with the area ratios of the stent lumen slice and vessel lumen slice.

flow rate ratios in the stented geometries are higher by 12.3%. The disparity is the highest at slice number 3 where 16.9% more flow passes through the stented lumen slice in the stented geometry. These ratio differences clearly show that the stent, although porous in structure, is significantly ‘funneling’ the flow within its bounds similar to flow-diverter devices which are used in the treatment of intracranial aneurysms (Brinjikji et al., 2013).

3.3. Impact of the malapposition on the wall shear stress

To understand the effect of the funneling of flow within the malapposed stent on the wall shear stress (WSS) of the vessel wall, various WSS metrics were plotted on the surface of the vessel as shown in Fig. 6. The TAWSS, which is the cycle-averaged wall shear stress magnitude,

was calculated using Eq. 1 within which $\vec{\tau}_w$ represents the WSS vector and T represents the time for one complete cardiac cycle. The TAWSS contour distribution is generally similar in both the stented and stent-absent geometries. A large high TAWSS region occurs at the sides of the anastomosis region due to the confluence of the two inlets. These high TAWSS values on the sides of the vessels continue to reduce as the flow reaches the venous outlet. Both geometries show a low TAWSS region in the vein close to the heel of the anastomosis, however, the low TAWSS region is larger in the stent-absent geometry compared to that of the stented geometry. When comparing the TAWSS contours with the velocity magnitude slices shown in Fig. 4, the reason for the larger low TAWSS region becomes clearer. As noted with the velocity contours in Fig. 4, the low velocity region in the heel of the vein of the stent-absent geometry is much larger than that of the stented geometry and this behaviour translates to the extent of the low TAWSS region in both cases.

$$TAWSS = \frac{1}{T} \int_0^T |\vec{\tau}_w| dt \quad (1)$$

$$OSI = 0.5 \left(1 - \frac{\frac{1}{T} \left| \int_0^T \vec{\tau}_w dt \right|}{TAWSS} \right) \quad (2)$$

The Oscillatory Shear Index (OSI), which gives a measure of the directional change of the WSS vector during a cardiac cycle (He and Ku, 1996), was calculated using Eq. 2 and plotted using contour bands as seen in Fig. 6. The distribution of OSI across both geometries largely remains at zero. However, at the heel of the vein in both geometries, there is a region of high OSI. This region is much larger in the stent-absent geometry, within which a large ring of high OSI occurs. Another location that shows high OSI is at the toe of the anastomosis region close to the DA (see Fig. 2 for annotated locations of the AVF) in

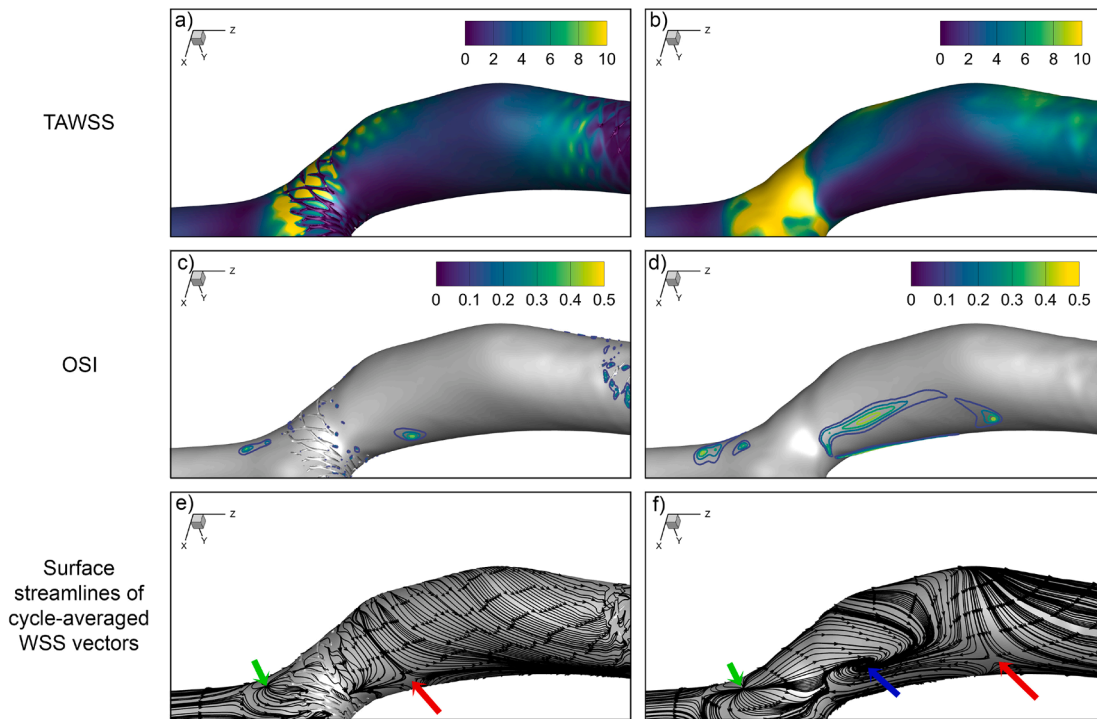


Fig. 6. WSS metrics across the stented (a, c and e) and stent-absent (b, d and f) AVF geometries. The distribution of TAWSS is shown in the contour plots of subfigures a and b. The distribution of OSI is shown in the contour band plots of subfigures c and d. The cycle-averaged WSS vectors are displayed using surface streamlines in subfigures e and f.

both geometries, however, the region is much narrower in the stent-absent geometry.

Finally, the cycle-averaged WSS vectors were used to plot surface streamlines on the AVFs as seen in Fig. 6. A clear reattachment point (annotated with red arrows) is seen in both geometries, and it coincides with the point at which the high OSI is observed. A noteworthy aspect of the reattachment point in the stent-absent geometry is that it is encountered much further down the vein (approximately 6mm further) in the stent-absent geometry resulting in a larger recirculation zone. Furthermore, a streamline focus (annotated with a blue arrow) is noted closer to the heel of the vein, only in the stent-absent geometry. Similar to the previous observations where the OSI distribution and streamline features overlap, at the anastomosis close to the DA where high OSI was observed, the streamline node point (as annotated with the green arrow) is observed (Perry and Chong, 1987).

The funnelling effect of the stent decreases the extent of vessel wall regions with high OSI and low TAWSS while also reducing other complex WSS behaviour. Regions of high OSI coupled with low TAWSS are known to encounter intimal thickening (Ku et al., 1985) and disturbed flow in these regions could be promoting inflammatory cell responses (Wang et al., 2013), leading to non-uniform remodelling and stenosis development (Cunnane et al., 2017). Therefore, the malapposed stent implantation alleviates the aforementioned adverse conditions within the vein to some degree, potentially reducing the risk of initiating intimal thickening.

The study is limited by the analysis of a single patient case, using a detailed benchtop methodology to obtain the stent features. Therefore, it is unlikely that the findings of this study will enable change in clinical practice, however, the significant observations of this study signal the necessity to progress these methodologies to larger cohorts to understand the level of consistency across varying subjects.

4. Conclusion

A numerical simulation of the blood flow within a patient-specific AVF was conducted to assess the impact of the juxta-anastomotic stent implantation treatment on the bulk flow within the vasculature. Micro-CT imaging of the stented benchtop AVF phantom was used to gain the stent features and the vessel lumen. An important feature that was apparent in the stented geometry was the malapposition of the stent close to the heel of the anastomosis, providing the opportunity to assess the impact of the stent malapposition by comparing the flow within an AVF model with and without the presence of a stent.

Visualisation of the flow streamlines and the velocity magnitude contours showed spiralling flow features in the anastomosis region of both models. A large recirculating low velocity region was observed at the heel of the anastomosis in the stent-absent geometry which has also been observed and predicted in other studies. However, the equivalent region in the stented geometry is much smaller. A second low velocity region was present at the lower regions within the stent encapsulated area, coupled with a high velocity region which was sustained further down the vein. These observations suggested the funnelling of flow within the stent encapsulated region which was further confirmed by assessing flow rate ratios, between the stent lumen and the vessel lumen, which were significantly higher in the stented geometry. The funnelling effect of the stent on the WSS was clearly evident, with a larger high OSI – low TAWSS region present in the stent-absent geometry along with more complex WSS behaviour in the vein.

The findings of this study show that, in this single representative patient-specific case, the severe malapposition of a stent yields favourable haemodynamic conditions that could prevent the initiation of inflammatory vessel wall mechanisms. The adverse flow behaviour is seen to be contained in the stent encapsulated region, thereby offsetting its impact away from the near-wall region. The suppression of adverse vessel wall forces potentially being the corollary of the degree of stent malapposition suggests that similar detailed studies on larger cohorts

could lead to better understanding of the complex effects of endovascular treatment.

Ethics approval

The patient's data was obtained after informed consent was given under the Low/Negligible Risk (LNR) Application with the Human Research Ethics Committee number 15/063 (LNR/16/POWH/7). The ethics for the related longitudinal study was updated under the Human Research Ethics Application ID 2018/ETH00577.

CRediT authorship contribution statement

Sanjiv Gunasekera: Conceptualization, Methodology, Software, Formal-analysis, Investigation, Data-curation, Writing-original-draft, Writing-review-editing. **Olivia Ng:** Investigation, Data-curation, Software, Writing-review-editing. **Shannon Thomas:** Conceptualization, Methodology, Investigation, Writing-review-editing, Supervision. **Ramon Varcoc:** Conceptualization, Methodology, Writing-review-editing, Supervision. **Charitha Silva:** Visualization, Methodology, Writing-review-editing, Supervision. **Tracie Barber:** Conceptualization, Methodology, Writing-review-editing, Supervision.

Declaration of Competing Interest

The authors declare that they have no known competing financial interests or personal relationships that could have appeared to influence the work reported in this paper.

Acknowledgements

Sanjiv Gunasekera and Olivia Ng are recipients of the Australian Government Research Training Program Scholarship and gratefully acknowledge this support.

Some of the data presented in this work was acquired by personnel and/or instruments at the Mark Wainwright Analytical Centre (MWAC) of UNSW Sydney, which is in part funded by the Research Infrastructure Programme of UNSW and National Imaging Facility (NCRIS).

This research includes computations using the computational cluster Katana supported by Research Technology Services at UNSW Sydney.

References

- Al-Jaishi, A.A., Liu, A.R., Lok, C.E., Zhang, J.C., Moist, L.M., 2017. Complications of the arteriovenous fistula: a systematic review. *J. Am. Soc. Nephrol.* 28, 1839–1850.
- ANZDATA, 2018. ANZDATA Registry. 41st Annual Report. The Australia and New Zealand Dialysis and Transplant Registry, Adelaide, Australia. Available at: URL: <http://www.anzdata.org.au>.
- Bozzetto, M., Ene-Iordache, B., Remuzzi, A., 2016. Transitional flow in the venous side of patient-specific arteriovenous fistulae for hemodialysis. *Ann. Biomed. Eng.* 44, 2388–2401.
- Brinjikji, W., Murad, M.H., Lanzino, G., Cloft, H.J., Kallmes, D.F., 2013. Endovascular treatment of intracranial aneurysms with flow diverters: a meta-analysis. *Stroke* 44, 442–447.
- Carroll, J.E., Colley, E.S., Thomas, S.D., Varcoc, R.L., Simmons, A., Barber, T.J., 2020. Tracking geometric and hemodynamic alterations of an arteriovenous fistula through patient-specific modelling. *Comput. Methods Programs Biomed.* 186, 105203.
- Chen, H.Y., Hermiller, J., Sinha, A.K., Sturek, M., Zhu, L., Kassab, G.S., 2009. Effects of stent sizing on endothelial and vessel wall stress: potential mechanisms for in-stent restenosis. *J. Appl. Physiol.* 106, 1686–1691.
- Chen, W.X., Poon, E.K., Thondapu, V., Hutchins, N., Barlis, P., Ooi, A., 2017. Haemodynamic effects of incomplete stent apposition in curved coronary arteries. *J. Biomech.* 63, 164–173.
- Chiu, J.J., Chien, S., 2011. Effects of disturbed flow on vascular endothelium: pathophysiological basis and clinical perspectives. *Physiol. Rev.* 91, 327–387.
- Cho, Y.I., Kenney, K.R., 1991. Effects of the non-newtonian viscosity of blood on flows in a diseased arterial vessel. Part 1: steady flows. *Biorheology* 28, 241–262.
- Colley, E., Carroll, J., Thomas, S., Varcoc, R.L., Simmons, A., Barber, T., 2018. A methodology for non-invasive 3-d surveillance of arteriovenous fistulae using freehand ultrasound. *IEEE Trans. Biomed. Eng.* 65, 1885–1891.

- Cunnane, C.V., Cunnane, E.M., Walsh, M.T., 2017. A review of the hemodynamic factors believed to contribute to vascular access dysfunction. *Cardiovasc. Eng. Technol.* 8, 280–294.
- Duque, J.C., Tabbara, M., Martinez, L., Cardona, J., Vazquez-Padron, R.I., Salman, L.H., 2017. Dialysis arteriovenous fistula failure and angioplasty: intimal hyperplasia and other causes of access failure. *Am. J. Kidney Dis.* 69, 147–151.
- Fu, N., Joachim, E., Yevzlin, A.S., Shin, J.I., Astor, B.C., Chan, M.R., 2015. A meta-analysis of stent placement vs. angioplasty for dialysis vascular access stenosis, in: *Seminars in Dialysis*, Wiley Online Library, pp. 311–317.
- Gimbrone Jr., M.A., García-Cardena, G., 2016. Endothelial cell dysfunction and the pathobiology of atherosclerosis. *Circul. Res.* 118, 620–636.
- Gunasekera, S., Ng, O., Thomas, S., Varcoe, R., de Silva, C., Barber, T., 2020. Tomographic piv analysis of physiological flow conditions in a patient-specific arteriovenous fistula. *Exp. Fluids* 61, 1–14.
- He, X., Ku, D.N., 1996. Pulsatile flow in the human left coronary artery bifurcation: average conditions. *J. Biomech. Eng.* 118, 74–82.
- Huang, E.P.Y., Li, M.F., Hsiao, C.C., Chen, H.Y., Wu, P.A., Liang, H.L., 2020. Undersized stent graft for treatment of cephalic arch stenosis in arteriovenous hemodialysis access. *Sci. Rep.* 10, 1–9.
- Ishibashi, H., Sunamura, M., Karino, T., 1995. Flow patterns and preferred sites of intimal thickening in end-to-end anastomosed vessels. *Surgery* 117, 409–420.
- Kharboubt, Z., Deplano, V., Bertrand, E., Legallais, C., 2010. Numerical and experimental study of blood flow through a patient-specific arteriovenous fistula used for hemodialysis. *Med. Eng. Phys.* 32, 111–118.
- Konner, K., Nonnast-Daniel, B., Ritz, E., 2003. The arteriovenous fistula. *J. Am. Soc. Nephrol.* 14, 1669–1680.
- Ku, D.N., Giddens, D.P., Zarins, C.K., Glagov, S., 1985. Pulsatile flow and atherosclerosis in the human carotid bifurcation. positive correlation between plaque location and low oscillating shear stress. *Arteriosclerosis Off. J. Am. Heart Association Inc.* 5, 293–302.
- Lok, C.E., Huber, T.S., Lee, T., Shenoy, S., Yevzlin, A.S., Abreo, K., Allon, M., Asif, A., Astor, B.C., Glickman, M.H., et al., 2020. Kdoqi clinical practice guideline for vascular access: 2019 update. *Am. J. Kidney Dis.* 75, S1–S164.
- McGah, P.M., Leotta, D.F., Beach, K.W., Aliseda, A., 2014. Effects of wall distensibility in hemodynamic simulations of an arteriovenous fistula. *Biomech. Model. Mechanobiol.* 13, 679–695.
- Perry, A.E., Chong, M.S., 1987. A description of eddying motions and flow patterns using critical-point concepts. *Annu. Rev. Fluid Mech.* 19, 125–155.
- Remuzzi, A., Ene-Iordache, B., 2013. Novel paradigms for dialysis vascular access: upstream hemodynamics and vascular remodeling in dialysis access stenosis. *Clin. J. Am. Soc. Nephrol.* 8, 2186–2193.
- Roy-Chaudhury, P., Sukhatme, V.P., Cheung, A.K., 2006. Hemodialysis vascular access dysfunction: a cellular and molecular viewpoint. *J. Am. Soc. Nephrol.* 17, 1112–1127.
- Stolic, R., 2013. Most important chronic complications of arteriovenous fistulas for hemodialysis. *Med. Principles Practice* 22, 220–228.
- Swinnen, J., Tan, K.L., Allen, R., Burgess, D., Mohan, I.V., 2015. Juxta-anastomotic stenting with aggressive angioplasty will salvage the native radiocephalic fistula for dialysis. *J. Vasc. Surg.* 61, 436–442.
- Tan, F., Soloperto, G., Bashford, S., Wood, N., Thom, S., Hughes, A., Xu, X., 2008. Analysis of flow disturbance in a stenosed carotid artery bifurcation using two-equation transitional and turbulence models. *J. Biomech. Eng.* 130.
- Thomas, S.D., Peden, S., Crowe, P., Varcoe, R.L., 2019. Interwoven nitinol stents to treat radiocephalic anastomotic arteriovenous fistula stenosis. *J. Endovasc. Therapy* 26, 394–401.
- Tonelli, M., Wiebe, N., Knoll, G., Bello, A., Browne, S., Jadhav, D., Klarenbach, S., Gill, J., 2011. Systematic review: kidney transplantation compared with dialysis in clinically relevant outcomes. *Am. J. Transpl.* 11, 2093–2109.
- TSANZ, 2019. *Clinical Guidelines for Organ Transplantation from Deceased Donors. Technical Report 1.3. The Transplantation Society of Australia and New Zealand.*
- Van Werkum, J.W., Heestermaas, A.A., Zomer, A.C., Kelder, J.C., Sutorp, M.J., Rensing, B.J., Koolen, J.J., Brueren, B.G., Dambrink, J.H.E., Hautvast, R.W., et al., 2009. Predictors of coronary stent thrombosis: the dutch stent thrombosis registry. *J. Am. College Cardiol.* 53, 1399–1409.
- Vijayaratham, P.R., O'Brien, C.C., Reizes, J.A., Barber, T.J., Edelman, E.R., 2015. The impact of blood rheology on drug transport in stented arteries: steady simulations. *PLoS One* 10.
- Wang, C., Baker, B.M., Chen, C.S., Schwartz, M.A., 2013. Endothelial cell sensing of flow direction. *Arterioscl. Thrombosis Vasc. Biol.* 33, 2130–2136.